Validating the improved angular resolution of the GRAPES-3 air shower array by observing the Moon shadow in cosmic rays

D. Pattanaik,[1,2] S. Ahmad,[3] M. Chakraborty,[1] S. R. Dugad,[1] U. D. Goswami,[4] S. K. Gupta,[1] B. Hariharan,[1] Y. Hayashi,[5] P. Jagadeesan,[1] A. Jain,[1] P. Jain,[6] S. Kawakami,[5] H. Kojima,[7] S. Mahapatra,[2] P. K. Mohanty,[1,*] R. Moharana,[8] Y. Muraki,[9] P. K. Nayak,[1] T. Nonaka,[10] A. Oshima,[7] B. P. Pant,[8] M. Rameez,[1] K. Ramesh,[1] L. V. Reddy,[1] S. Shibata,[7] F. Varsi,[6] and M. Zuberi[1]

(GRAPES-3 Collaboration)

[1]*Tata Institute of Fundamental Research, Homi Bhabha Road, Mumbai 400005, India*
[2]*Utkal University, Bhubaneshwar 751004, India*
[3]*Aligarh Muslim University, Aligarh 202002, India*
[4]*Dibrugarh University, Dibrugarh 786004, India*
[5]*Graduate School of Science, Osaka City University, Osaka 558-8585, Japan*
[6]*Indian Institute of Technology Kanpur, Kanpur 208016, India*
[7]*College of Engineering, Chubu University, Kasugai, Aichi 487-8501, Japan*
[8]*Indian Institute of Technology Jodhpur, Jodhpur 342037, India*
[9]*Institute for Space-Earth Environmental Research, Nagoya University, Nagoya 464-8601, Japan*
[10]*Institute for Cosmic Ray Research, Tokyo University, Kashiwa, Chiba 277-8582, Japan*

(Received 30 April 2022; accepted 13 July 2022; published 29 July 2022)

The Moon blocks cosmic rays, causing a deficit in their flux from its direction. Characterizing this Moon shadow is a technique used by cosmic ray air shower experiments to calibrate their angular resolution and validate the pointing accuracy. The GRAPES-3 air shower array, located in Ooty, India consists of an array of scintillator detectors and a large area muon telescope. It is sensitive to the measurement of cosmic ray and gamma ray induced showers in the TeV-PeV energy range. The timing measurements of the scintillator detectors were improved after upgrading the time-to-digital converters and coaxial cables in late 2012. The propagation delay of photomultiplier signal in coaxial cables were accurately determined on hourly basis using a random walk technique. The correction of shower front curvature for its dependence on the shower size and age together with accurate timing measurements led to a better angular resolution estimated using array division methods reported elsewhere [Jhansi *et al.*, J. Cosmol. Astropart. Phys. 07 (2020) 024]. In this paper, we discuss the validation of the angular resolution by observing the shadow of the Moon in cosmic ray flux using 3 years (2014 to 2016) of air shower data recorded during the postupgrade period. The angular resolution of the array was estimated to be $0.83° \pm 0.09°$ with a statistical significance of 9.1σ and pointing accuracy along the right ascension and declination directions were obtained to be $0.032° \pm 0.004°$ and $0.09° \pm 0.003°$ for showers of energy >5 TeV, containing about 95% of triggered showers. The angular resolution improves to $0.38° \pm 0.06°$ and $0.29° \pm 0.06°$ for energy >100 TeV and >200 TeV respectively. The results are consistent with the values obtained from array division methods and are comparable to several air shower arrays that are located at almost twice the altitude of GRAPES-3. The improved angular resolution together with the accurate pointing increases the ability of GRAPES-3 to detect multi-TeV gamma ray sources.

DOI: 10.1103/PhysRevD.106.022009

I. INTRODUCTION

The past two decades have witnessed tremendous progress in the field of gamma ray astronomy. Gamma rays are not deflected by the interstellar magnetic fields. Thus, their arrival direction can point to their source, enabling to use them as an effective probe for the origin of cosmic rays. Currently the ground based air shower experiments provide the only feasible way to study gamma ray sources above 100 TeV because of their large effective area, wide field of view and nearly 100% duty cycle. The air shower arrays such as Tibet ASγ [1], HAWC [2], and LHAASO [3,4] have observed several gamma ray sources in the recent past exceeding 100 TeV energy. These results

*pkm@tifr.res.in

have generated considerable excitement in the field since sub-PeV gamma rays could be linked to the source of PeV cosmic rays. Gamma ray observation at multi-TeV energies is challenging due to their extremely low flux and an overwhelming cosmic ray background of several orders of magnitude. Air shower arrays with good angular resolution and muon measurements could achieve a large rejection of the cosmic ray background. Good angular resolution can be achieved by installing detectors at high altitude location, keeping the interdetector separation to be as small as possible and making accurate measurements of the arrival time of the shower particles.

The angular resolution can be estimated using array division methods, i.e., dividing the array into subarrays consisting of left and right or even and odd numbered detectors [5]. However, accurate measurement of angular resolution can be obtained by observing the shadow of the Moon in the cosmic ray flux. Due to their charged nature, cosmic ray directions are randomized by the interstellar magnetic fields resulting in an isotropic distribution of their flux. The Moon blocks cosmic rays, preventing them from reaching the Earth. As seen from the Earth, the average angular radius of the Moon is 0.26°. However, it various over 10 to 15% during its orbital period of 27.3 days of the Moon. The shape and magnitude of the deficit provides a measure of the angular resolution of the array, whereas the location of the maximum deficit provides its pointing accuracy. This method was first proposed by Clark [6] and was afterwards used by various air shower experiments such as CYGNUS [7], Tibet ASγ [8], CASA [9], ARGO-YBJ [10], and HAWC [11] to estimate their angular resolutions. Underground experiments such as MACRO [12], SOUDAN [13], L3 [14], MINOS [15], IceCube [16] and ANTARES [17] have also used the shadow of the Moon in high energy muons for determining their angular resolutions.

In the past, the angular resolution of the GRAPES-3 scintillator array was estimated from the cosmic ray shadow of the Moon using 4 years of shower data spanning 2000–2003 [5]. Since then, the array has undergone several upgrades. These include: (1) upgrade of the scintillator detectors from a traditional design to a wavelength shifting (WLS) fiber based design [18], (2) replacement of commercial time to digital converters (TDC) with an in-house developed 32-channel high performance TDC called as HPTDC [19], (3) using low attenuation coaxial cables namely 5D2V for better timing measurements, and (4) accurate measurement of time offsets with a random walk technique [20]. Further, the curvature in the shower front and its dependence on shower size (N_e) and age (s) was obtained [20]. This is in contrast to the earlier analysis where a constant curvature value (0.215 ns m^{-1}) was used [5]. All these helped to achieve a major improvement in the angular resolution as determined and demonstrated using array division methods [20]. In this paper, we present the validation of the angular resolution and determination of pointing accuracy of the array using Moon shadow technique.

II. THE GRAPES-3 EXPERIMENT

The GRAPES-3 is an air shower experiment located at Ooty (11.4°N, 76.7°E and 2200 m a.s.l.) in Tamil Nadu, India. Its near equatorial location provides a unique opportunity to study gamma ray sources, in both Northern as well as the Southern hemispheres. The array started taking data in 2000 with 217 plastic scintillator detectors of 1 m^2 area each placed with an inter-detector separation of 8 m [21]. These detectors are based on a traditional cone type design wherein the photon collection is by a photomultiplier tube located 60 cm above the scintillators. Later the array was upgraded with plastic scintillator detectors read out using wavelength shifting fibers [18,22]. The array currently consists of 400 scintillator detectors spread over an area of 25000 m^2. A large area (560 m^2) muon telescope is located near the periphery of the array as shown in Fig. 1. This consists of 16 modules of 35 m^2 area each, used to measure the muon content in the air shower [23]. Each scintillator detector is designed to record the densities and arrival times of the particles in the shower using a charge sensing analog to digital converter (qADC) and TDC respectively. In late 2012, the commercial TDCs were replaced with an in-house developed 32 channel high performance TDC (HPTDC), based on an ASIC developed by microelectronics group at CERN, Geneva [19]. The HPTDCs were operated with a digitization accuracy of 195 ps per count and in a dynamic range of 3.5 μs, over which it has exhibited an excellent linearity.

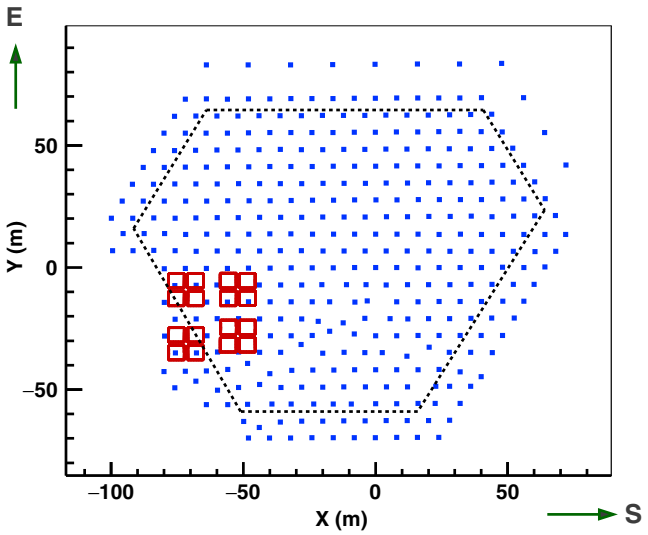

FIG. 1. Schematic diagram of the GRAPES-3 experiment with the scintillator detectors represented by blue solid square and the muon telescope modules represented by red open square. The fiducial area is bounded by dash lines.

III. ANALYSIS AND RESULTS

For this analysis, we have used three years of shower data, recorded between 1 January 2014 and 31 December 2016, comprising total 2.98×10^9 events with a live time of 994.1 days. The showers were reconstructed using the Nishimura-Kamata-Greisen (NKG) lateral distribution function [24,25]. A log-likelihood method using the MINUIT algorithm [26] was used for the minimization [27]. Various shower parameters of the shower such as core location (X_c, Y_c), N_e, and s were obtained from the minimization. The curvature of the shower front was corrected based on N_e and s which is described elsewhere [20]. Next, a plane fit to the relative arrival times of shower particles recorded at different scintillator detectors is performed to obtain the direction of the shower in terms of zenith angle (θ) and azimuth angle (ϕ). Five more iterations for the direction reconstruction were performed after identifying and removing detectors recorded with significant deviations from the expected arrival times. For this, the root mean square (RMS) deviation was calculated by comparing the observed arrival times with the expected arrival times using the parameters from the plane fit. A detailed description of the outlier removal procedure can be found elsewhere [20]. A detector was identified as outlier detector if the deviation of the arrival time from the expected front was $>(2 \times \mathrm{RMS})$ for $\log_{10}(N_e) \leq 4.1$ and $>(1.5 \times \mathrm{RMS})$ for $\log_{10}(N_e) > 4.1$. Figure 2 shows the results of angular resolution for various iterations. It can be seen that the removal of outliers significantly improved the angular resolution as determined using the left-right array division method [20]. In this method, the array is divided into a "left" and a "right" subarray. For each shower, a line joining its core and the array center is used as the dividing line for the two subarrays. Even though the improvement in angular resolution is significant after the first round of outlier removal, the optimum number of iterations was found to be two.

Several criteria were imposed to select high quality data. Showers with successful NKG fit, as judged by the convergence of the fit matrix were selected. Very high energy showers with cores landing outside of the array could be misreconstructed to have their cores lying inside the array, due to partial information recorded by the array. To reduce the contamination from such showers, only the reconstructed cores within a fiducial area ($\sim$14500 m^2) enclosed by the dashed line as shown in Fig. 1 were selected. This excludes the two outermost rings of detectors. A further cut was imposed on the shower age parameter "s," to be between 0.2 and 1.8. Only events with reconstructed $\theta < 40°$ are selected. After imposing all these criteria, $\sim 1.65 \times 10^9$ showers remained for further analysis. The angular resolution obtained using the left-right method separately for years 2014, 2015 and 2016 are shown in Fig. 3. The resolutions are very similar between the years, demonstrating that the quality of the data remained almost unchanged.

To find the relationship between the shower size and its primary energy, we employed a Monte Carlo simulation of proton primaries using the CORSIKA v7.4009 package with QGSJET II-04 interaction model for high-energy and FLUKA interaction model for low energy air showers [28,29]. The same selection criteria as employed on observed data were used for this Monte Carlo dataset. The primary energy (E_T) was divided into differential logarithmic bins of $10^{0.2}$ width. The median value of the primary energy as plotted against the median shower size for different zenith angles. As shown in Fig. 4, the range in $\log_{10}(N_e)$ was divided into two regions. For the lower shower size ($\log_{10}(N_e) \leq 4.1$), the relationship between shower size and primary energy is obtained by fitting a

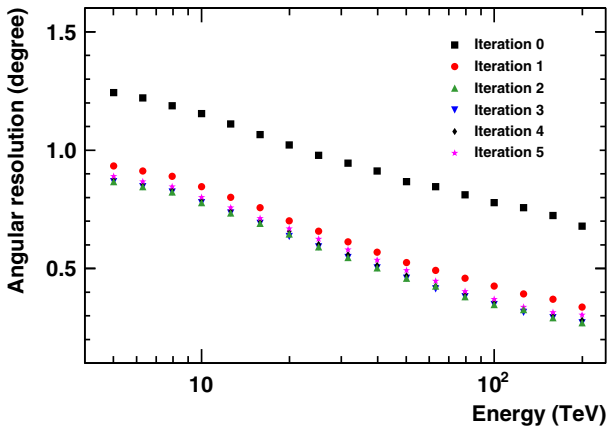

FIG. 2. Angular resolution for the GRAPES-3 array obtained using left-right method without removal of outliers (Iteration 0) and removal of outliers (Iteration 1 to 5).

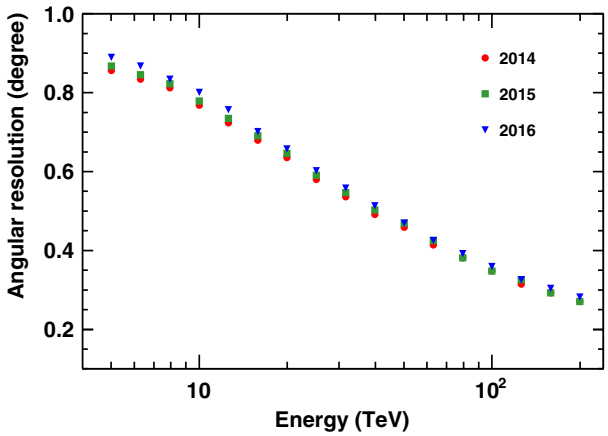

FIG. 3. Angular resolution for the GRAPES-3 array obtained using left-right method after second iteration of outlier removal for the year 2014, 2015 and 2016.

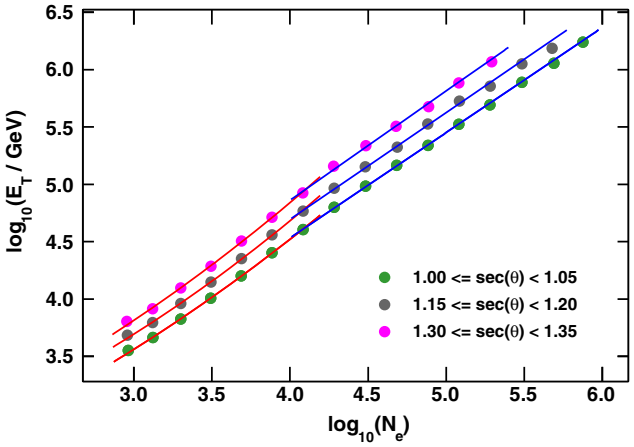

FIG. 4. Log of true energy (E_T) of the showers plotted as a function of log of shower size (N_e) for different zenith angle (θ) bins. The lines represent quadratic polynomial fit up to $\log_{10}(N_e) \leq 4.1$ and linear fit beyond it.

quadratic function while a linear function is used for higher shower size ($\log_{10}(N_e) > 4.1$).

$$\log_{10}(E_T/\mathrm{GeV}) = a_0 + a_1 \times \log_{10}(N_e) + a_2 \times (\log_{10}(N_e))^2$$
$$\log_{10}(E_T/\mathrm{GeV}) = b_0 + b_1 \times \log_{10}(N_e) \quad (1)$$

Here a_0, a_1, and a_2 are parameters for the quadratic region ($\log_{10}(N_e) \leq 4.1$) while b_0 and b_1 are parameters obtained from the fit for the linear region ($\log_{10}(N_e) > 4.1$). The parameters thus obtained are used for converting the experimental N_e into energy on an event by event basis. For clarity, only plots for three zenith angle (θ) bins are shown in Fig. 4. The energy-size relation was estimated for showers up to 45° zenith angle.

The Moon follows a complicated trajectory in the sky. The position of the Moon in local coordinates of zenith and azimuth (θ, ϕ) for the GRAPES-3 location was calculated using routines from Astropy [30,31]. The angle ψ between shower direction (θ_E, ϕ_E) and the direction of the Moon (θ_M, ϕ_M) was calculated for the time stamp of the shower event which is recorded to 100 ns accuracy. The events were binned into 14 annular concentric bins of width 0.25° in ψ as illustrated in Fig. 5. The bin width is approximately equal to the angular radius of the Moon which is 0.26°.

The number of events observed in each of the annular bins increases with increase in angular distance from the centre of the Moon, due to the increasing solid angle covered by each bin. For each annular bin, the total number of events is rescaled by the ratio of the solid angles of the central annular bin and the bin in consideration, to obtain the event density. Hence the event density can be expressed by Eq. (2),

$$N_{\Omega_i} = \frac{N_i}{\Omega_i} \times \Omega_\circ \quad (2)$$

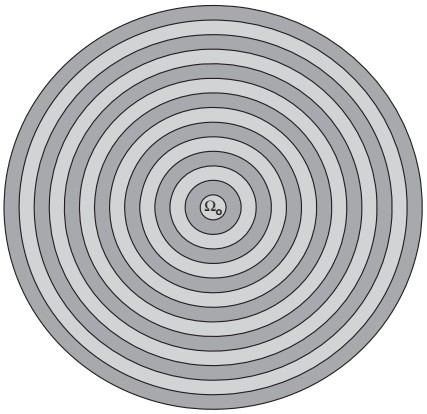

FIG. 5. An illustration of the annular regions of equal angular width of 0.25° around the Moon. Here the central region depicts a circular region of angular radius 0.25° which is comparable to the angular radius of the Moon.

where N_{Ω_i} is the event density and N_i is the number of events observed in ith annular bin. Ω_i is the solid angle for the ith annular bin and $\Omega_\circ$ is the solid angle of the central annular bin. If ψ is the incident angle measured from the center of the Moon, then Ω_i and $\Omega_\circ$ can be expressed by Eq. (3).

$$\Omega_i = 2\pi \int_{\psi_i}^{\psi_{i+1}} \sin(\psi) d\psi \approx \pi(\psi_{i+1}^2 - \psi_i^2)$$
$$\Omega_\circ = 2\pi \int_0^{\psi_0} \sin(\psi) d\psi \approx \pi(\psi_0)^2 \quad (3)$$

The events were binned into a histogram with a bin width of 0.25° in ψ for a range 0 to 3.5°. The annular binning was performed for different integral energy bins varying from 10^3 GeV to $10^{5.5}$ GeV in steps of bin size of $10^{0.1}$ GeV.

Ten different background regions in the sky around the Moon (hereby called fake Moon regions) were selected such that they are located at 6° successive shifts (±6°, ±12°, ±18°, ±24°, and ±30°) in the azimuth direction from the Moon. The fake Moon regions were selected with the same zenith angle of the real Moon. Any systematic effect originating from the detectors, atmospheric parameters or zenith angle dependence will reflect both in the original and fake Moon data. Therefore, after the background subtraction, the residual effect is expected to be only due to the Moon shadow effect. Average event density of 10 background regions were calculated.

The deficit of cosmic ray events from the direction of the Moon relative to the background was obtained using Eq. (4) as described in [16],

$$\frac{\Delta N_i}{\langle N \rangle} = \frac{N_i^{\mathrm{on}} - \langle N_i^{\mathrm{off}} \rangle}{\langle N_i^{\mathrm{off}} \rangle} \quad (4)$$

while the uncertainty in the deficit was calculated by,

$$\sigma_{\Delta N/\langle N\rangle} = \frac{N_i^{\rm on}}{\langle N_i^{\rm off}\rangle}\sqrt{\frac{1}{N_i^{\rm on}} + \frac{1}{n\langle N_i^{\rm off}\rangle}} \tag{5}$$

where $N_i^{\rm on}$ is the number of events in the ith bin for the real Moon region and $\langle N_i^{\rm off}\rangle$ is the average number of events in the ith bin obtained from the fake Moon regions and $n = 10$ is the number of fake Moon regions chosen for the analysis. We increased $n = 10$ to $n = 20$ by selecting the azimuth angle up to $\pm 60°$ to check if there is any bias arising due to background selection. However, the results remained unchanged. The background subtracted results for $n = 10$ are shown in Fig. 6 for four different integral energy bins (>5 TeV, >50 TeV, >100 TeV, and >200 TeV). The error bar on each data point represents the statistical uncertainty. The uncertainties gradually become smaller away from the direction of the Moon due to increasing statistics from the increasing solid angle. The fractional deficit of the events in the direction from the center of the Moon is clearly visible for each energy bin and it increases with energy. To estimate the deficit as well as to determine angular resolution of each energy bin, the data were fitted with a monovariate 2-dimensional Gaussian function given by Eq. (6) as used in [16],

$$N(\psi) = N_0 \frac{\psi_M^2}{2\sigma_\psi^2} e^{-\frac{\psi^2}{2\sigma_\psi^2}} \tag{6}$$

where ψ is the space angle measured from the center of the Moon, ψ_M is the angular radius of the Moon and σ_ψ represents the angular resolution of the array. From the Moon tracking while considering only the GRAPES-3 observation period, the average value of ψ_M obtained for 2014, 2015, and 2016 are 0.262°, 0.263°, and 0.263° respectively. A value of 0.26° was used in the fit. For optimum signal from a point source for a detector with a Gaussian point spread function, the opening angle selected is 1.58 times of the angular resolution [32]. Therefore, the significance (S) was calculated from the events [Eq. (7)] observed within $1.58 \times \sigma_\psi$.

$$S = \left(\frac{\Delta N}{\sqrt{N_b}}\right)_{\psi \le 1.58\times\sigma_\psi} \tag{7}$$

In Eq. (7), ΔN represents the sum of the deficits, i.e., $\Sigma_i(N_i^{\rm on} - \langle N_i^{\rm off}\rangle)$ and N_b is the sum of the average background events up to $\psi \le 1.58 \times \sigma_\psi$. For energy >5 TeV, the σ_ψ was obtained to be 0.83°. Within $1.58 \times \sigma_\psi = 1.3°$, a total of 346188 numbers of events were observed from the Moon region ($N^{\rm on}$) and 351582 events were observed from the fake Moon regions ($N^{\rm off}$). Hence the significance (S) is calculated to be $(351582 - 346188)/\sqrt{351582} \approx 9.1\sigma$.

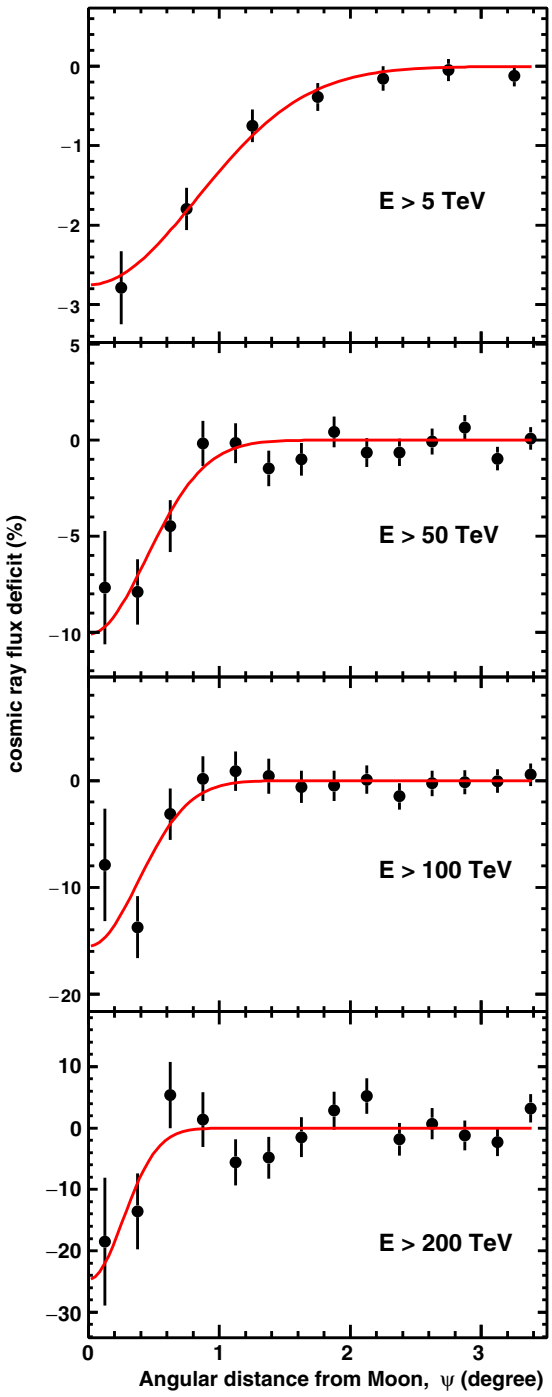

FIG. 6. Deficit of cosmic ray events from the real Moon region relative to fake Moon regions for four different energy thresholds, i.e. 5 TeV, 50 TeV, 100 TeV, and 200 TeV as a function of the angle from the Moon center. A 2-dimensional monovariate Gaussian fit to the deficit profile is represented by the red line.

A summary of the results from the fit are given in Table I.

Another important objective of observing the Moon shadow is to find out the absolute pointing accuracy of the detector. At first, the local coordinates (θ and ϕ) of the

TABLE I. Summary of the results obtained after fitting the deficit plot using Eq. (6).

Energy (TeV)	Angular resolution	Significance
5	$0.83° \pm 0.09°$	9.1σ
50	$0.44° \pm 0.07°$	5.4σ
100	$0.38° \pm 0.06°$	4.5σ
200	$0.29° \pm 0.06°$	3.1σ

events were transformed into equatorial coordinates, i.e., right ascension (α) and declination (δ). The difference in δ between event and the Moon ($\Delta\delta = \delta_{\text{event}} - \delta_{\text{Moon}}$) was then plotted against the difference in α ($\Delta\alpha = \alpha_{\text{event}} - \alpha_{\text{Moon}}$) as a HEALPix map [33]. By subtracting the equatorial coordinates of the Moon from the events, Moon position was eventually transformed to the center of the map (i.e., $\Delta\alpha = 0°$, $\Delta\delta = 0°$). To enhance the Moon shadow visualization, the map was then smoothed using top hat function with a smoothing radius same as the angular resolution. The resultant plot is shown in Fig. 7 for energy >5 TeV.

A grid division method was adopted to find the position of maximum deficit that would describe the pointing accuracy. In this method, to locate the pointing in α, a rectangular area engulfing the Moon with a dimension of 2° (−1° to 1°) along $\Delta\delta$ and 4° (−2° to 2°) along $\Delta\alpha$ was selected. The rectangular area was further divided into 20 bins of equal width (0.2°) along $\Delta\alpha$ resulting into 20 different grids having identical dimension of $1° \times 0.2°$ ($\Delta\delta \times \Delta\alpha$). The mean relative deficit in each grid was plotted against the corresponding value of $\Delta\alpha$ (see Fig. 8).

The variation of the mean relative deficit with $\Delta\alpha$ was fitted with a quadratic polynomial [Eq. (8)]. From the fitted parameters, the position of the minima and the error were

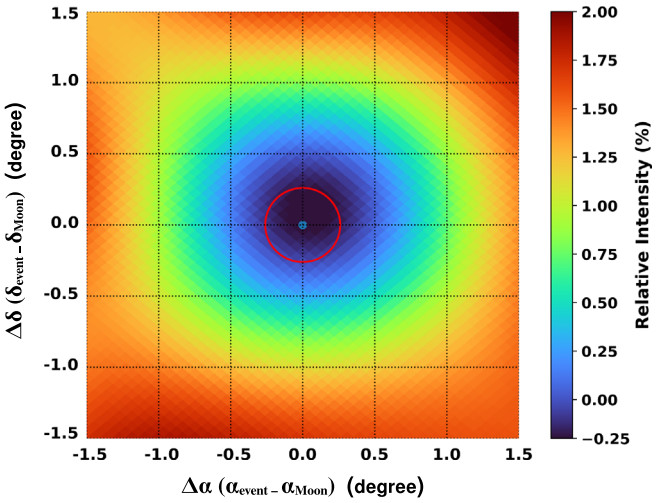

FIG. 7. HEALPix map of the Moon shadow for the showers of energy above 5 TeV. The blue marker represents the center ($\Delta\alpha = 0°, \Delta\delta = 0°$) and the red circle around it is an ideal representation of the Moon (angular radius = 0.26°).

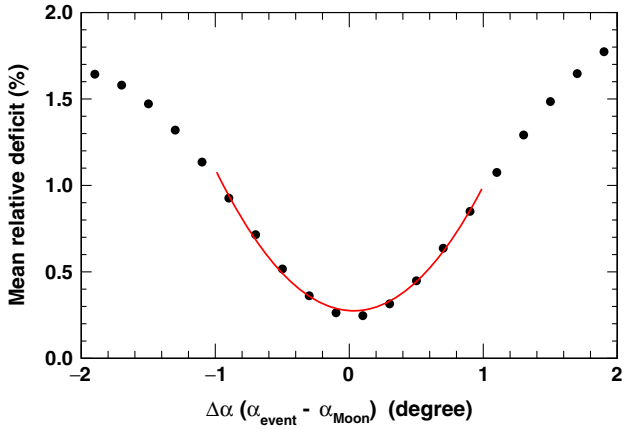

FIG. 8. Variation of mean relative deficit as a function of $\Delta\alpha$ for events above 5 TeV. The variation was fitted with a quadratic function to obtain the position of minimum. The minimum was found at $\Delta\alpha = 0.032° \pm 0.004°$ which describes the pointing of the detector along α.

calculated by using Eq. (9) and Eq. (10) respectively. For events with energy above 5 TeV, the minima along $\Delta\alpha$ was obtained to be $0.032° \pm 0.004°$ which was considered as the pointing in α. Following the same strategy, the pointing in δ was obtained to be $0.09° \pm 0.003°$.

$$f(x) = a + bx + cx^2 \tag{8}$$

$$x_{\text{minima}} = \frac{-b}{2c} \tag{9}$$

$$\epsilon_x = \left(\frac{b}{2c}\right) \times \sqrt{\left(\frac{\Delta b}{b}\right)^2 + \left(\frac{\Delta c}{c}\right)^2} \tag{10}$$

IV. DISCUSSION AND SUMMARY

Three years of air shower data collected by the GRAPES-3 air shower array between 1 January 2014 and 31 December 2016 were analyzed to study the angular resolution. The curvature in the shower front was corrected for its dependence on shower size and age during the direction reconstruction. The angular resolutions obtained from the observation of the Moon shadow and left-right method for different integral energy bins are shown in Fig. 9. Further, the angular resolution obtained earlier from the same experiment using data from 2000 to 2003 is also shown in the same figure for comparison [5]. It is to be noted that the earlier analysis was performed using a constant curvature of 215 ps.m^{-1}. The angular resolution obtained from the Moon shadow method varies from 0.83° at energy >5 TeV to 0.29° at energy >200 TeV. The values are consistent with the left-right method within the statistical uncertainties. However, these results show a significant improvement as compared to the earlier analysis [5]. The improvement is much higher at low energy. For example at

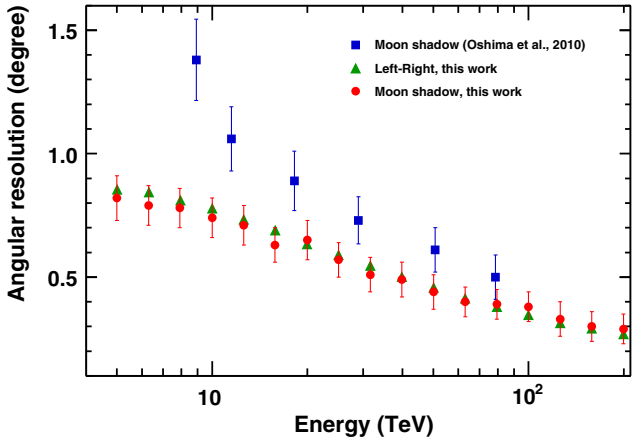

FIG. 9. The angular resolution of the GRAPES-3 air shower array from the analysis of 2014 to 2016 data using left-right array division method is represented by green triangle and from the Moon shadow method is represented by red circle. The results of earlier Moon shadow analysis using 2000 to 2003 data is represented by blue square.

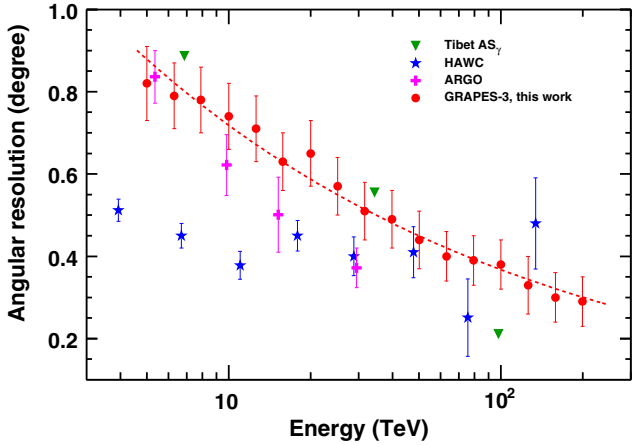

FIG. 10. The angular resolution of the GRAPES-3 air shower array obtained from Moon shadow analysis compared with other air shower arrays such as ARGO [34], Tibet ASγ [1,8], HAWC [11]. The GRAPES-3 data points are fitted with $k \times E^{\gamma}$ where E is the energy. The fit parameters are $k = 1.40 \pm 0.13$ and $\gamma = -(0.29 \pm 0.03)$.

10 TeV, the improvement is about 75%. The pointing accuracy along α and δ were obtained to be $0.032° \pm 0.004°$ and $0.09° \pm 0.003°$ respectively for energy above 5 TeV. These are within the statistical error of angular resolution for this energy.

In Fig. 10, the angular resolution of GRAPES-3 obtained from the observation of the Moon shadow is compared with other air shower experiments such as ARGO [34], Tibet AS$_\gamma$ [1,8], and HAWC [11]. All these experiments are located at an altitude of about 4100 to 4400 m which is approximately twice the altitude of the GRAPES-3. Calculations presented in the paper [35] show that a factor improvement in the angular resolution can be gained for these experiments as compared to GRAPES-3 from altitude consideration. The results suggest that other experiments may achieve improvements in their angular resolution by adopting similar analysis techniques as GRAPES-3, in particular, the shower front curvature corrections depending on the size and age of the shower. The significant improvement in the angular resolution opens up the opportunity for the GRAPES-3 experiment to detect high energy gamma ray sources extending to PeV energies.

ACKNOWLEDGMENTS

We are grateful to D. B. Arjunan, V. Jeyakumar, S. Kingston, K. Manjunath, S. Murugapandian, S. Pandurangan, B. Rajesh, V. Santoshkumar, M. S. Shareef, C. Shobana, and R. Sureshkumar for their role in efficient running of the experiment. We acknowledge support of the Department of Atomic Energy, Government of India, under Project Identification No. RTI4002. This work was partially supported by grants from Chubu University, ISEE of Nagoya University, and ICRR of Tokyo University, Japan.

[1] M. Amenomori *et al.* (Tibet ASγ Collaboration), First Detection of Photons with Energy beyond 100 TeV from an Astrophysical Source, Phys. Rev. Lett. **123**, 051101 (2019).
[2] A. U. Abeysekara *et al.* (HAWC Collaboration), Measurement of the Crab Nebula spectrum past 100 TeV with HAWC, Astrophys. J. **881**, 134 (2019).
[3] F. Aharonian *et al.* (LHAASO Collaboration), Observation of the Crab Nebula with LHAASO-KM2A—a performance study, Chin. Phys. C **45**, 025002 (2021).
[4] Z. Cao *et al.* (LHAASO Collaboration), Ultrahigh-energy photons up to 1.4 petaelectronvolts from 12γ-ray Galactic sources, Nature (London) **594**, 33 (2021).
[5] A. Oshima *et al.* (GRAPES-3 Collaboration), The angular resolution of the GRAPES-3 array from the shadows of the Moon and the Sun, Astropart. Phys. **33**, 97 (2010).
[6] G. W. Clark, Arrival directions of cosmic-ray air showers from the northern sky, Phys. Rev. **108**, 450 (1957).
[7] D. E. Alexandreas *et al.*, Observation of shadowing of ultrahigh-energy cosmic rays by the Moon and the Sun, Phys. Rev. D **43**, 1735 (1991).
[8] M. Amenomori *et al.* (Tibet ASγ Collaboration), Cosmic-ray deficit from the directions of the Moon and the Sun detected with the Tibet air-shower array, Phys. Rev. D **47**, 2675 (1993).

[9] A. Borione *et al.*, Observation of the shadows of the Moon and Sun using 100 TeV cosmic rays, Phys. Rev. D **49**, 1171 (1994).
[10] B. Bartoli *et al.* (ARGO-YBJ Collaboration), Measurement of the cosmic ray antiproton/proton flux ratio at TeV energies with the ARGO-YBJ detector, Phys. Rev. D **85**, 022002 (2012).
[11] R. Alfaro *et al.* (HAWC Collaboration), All-particle cosmic ray energy spectrum measured by the HAWC experiment from 10 to 500 TeV, Phys. Rev. D **96**, 122001 (2017).
[12] M. Ambrosio *et al.* (MACRO Collaboration), Observation of the shadowing of cosmic rays by the Moon using a deep underground detector, Phys. Rev. D **59**, 012003 (1998).
[13] J. H. Cobb *et al.* (The Soudan 2 Collaboration), Observation of a shadow of the Moon in the underground muon flux in the Soudan 2 detector, Phys. Rev. D **61**, 092002 (2000).
[14] P. Achard, O. Adriani, M. Aguilar-Benitez, M. van den Akker, J. Alcaraz, G. Alemanni, J. Allaby, A. Aloisio, M. G. Alviggi, and H. Anderhub (The L3 Collaboration), Measurement of the shadowing of high-energy cosmic rays by the Moon: A search for TeV-energy antiprotons, Astropart. Phys. **23**, 411 (2005).
[15] P. Adamson *et al.*, Observation in the MINOS far detector of the shadowing of cosmic rays by the sun and moon, Astropart. Phys. **34**, 457 (2011).
[16] M. G. Aartsen *et al.* (IceCube Collaboration), Observation of the cosmic-ray shadow of the Moon with IceCube, Phys. Rev. D **89**, 102004 (2014).
[17] A. Albert, D. G. Espinosa, R. Jaarsma, and G. Tetlalmatzi-Xolocotzi, The cosmic ray shadow of the Moon observed with the ANTARES neutrino telescope, Eur. Phys. J. C **78**, 1 (2018).
[18] P. K. Mohanty, S. R. Dugad, and S. K. Gupta (GRAPES-3 Collaboration), Monte Carlo code G3sim for simulation of plastic scintillator detectors with wavelength shifter fiber readout, Rev. Sci. Instrum. **83**, 043301 (2012).
[19] J. Christiansen, *HPTDC High Performance Time to Digital Converter*, Technical Report (CERN, Geneva, 2004), https://cds.cern.ch/record/1067476.
[20] V. B. Jhansi *et al.* (GRAPES-3 Collaboration), The angular resolution of GRAPES-3 EAS array after improved timing and shower front curvature correction based on age and size, J. Cosmol. Astropart. Phys. 07 (2020) 024.
[21] S. K. Gupta *et al.* (GRAPES-3 Collaboration), GRAPES-3-A high-density air shower array for studies on the structure in the cosmic-ray energy spectrum near the knee, Nucl. Instrum. Methods Phys. Res., Sect. A **540**, 311 (2005).
[22] P. K. Mohanty *et al.* (GRAPES-3 Collaboration), Measurement of some EAS properties using new scintillator detectors developed for the GRAPES-3 experiment, Astropart. Phys. **31**, 24 (2009).
[23] Y. Hayashi *et al.* (GRAPES-3 Collaboration), A large area muon tracking detector for ultra-high energy cosmic ray astrophysics-the GRAPES-3 experiment, Nucl. Instrum. Methods Phys. Res., Sect. A **545**, 643 (2005).
[24] K. Kamata and J. Nishimura, The lateral and the angular structure functions of electron showers, Prog. Theor. Phys. Suppl. **6**, 93 (1958).
[25] K. Greisen, Cosmic ray showers, Annu. Rev. Nucl. Sci. **10**, 63 (1960).
[26] F. James *et al.*, MINUIT: Function Minimization and Error Analysis Reference Manual (1998), CERN Program Library Long Writeups, https://cds.cern.ch/record/2296388.
[27] H. Tanaka *et al.* (GRAPES-3 Collaboration), Studies of the energy spectrum and composition of the primary cosmic rays at 100–1000 TeV from the GRAPES-3 experiment, J. Phys. G **39**, 025201 (2012).
[28] D. Heck *et al.*, A Monte Carlo code to simulate extensive air showers, Rep. FZKA **6019** (1998), https://inspirehep.net/literature/469835.
[29] S. Ostapchenko, QGSJET-II: Towards reliable description of very high energy hadronic interactions, Nucl. Phys. **B151**, 143 (2006).
[30] T. P. Robitaille *et al.* (The Astropy Collaboration), Astropy: A community Python package for astronomy, Astron. Astrophys. **558**, A33 (2013).
[31] A. M. Price-Whelan *et al.* (The Astropy Collaboration), The astropy project: Building an open-science project and status of the v2.0 core package, Astron. J. **156**, 123 (2018).
[32] L. J. Graham, Ultra high energy gamma ray point sources and cosmic ray anisotropy, Doctoral thesis, Durham University, 1994, http://etheses.dur.ac.uk/5594/.
[33] K. M. Gorski, E. Hivon, A. J. Banday, B. D. Wandelt, F. K. Hansen, M. Reinecke, and M. Bartelmann, HEALPix: A framework for high-resolution discretization and fast analysis of data distributed on the sphere, Astrophys. J. **622**, 759 (2005).
[34] G. Aielli *et al.* (ARGO-YBJ Collaboration), Highlights from the ARGO-YBJ experiment, Nucl. Instrum. Methods Phys. Res., Sect. A **661**, S50 (2012).
[35] W. Hofmann, On angular resolution limits for air shower arrays, Astropart. Phys. **123**, 102479 (2020).